

1

2 **Hyperedge bundling: A practical solution to spurious** 3 **interactions in MEG/EEG source connectivity analyses**

4

5

6

7

8 **Sheng H. Wang^{1,2,3}, Muriel Lobier¹, Felix Siebenhühner^{1,2}, Satu Palva^{1,3}, J. Matias Palva¹**

9 *1. Neuroscience Center, University of Helsinki, Finland*

10 *2. Doctoral Programme Brain & Mind, University of Helsinki, Finland*

11 *3 BioMag laboratory, HUS Medical Imaging Center, Helsinki, Finland*

12

13

14

15

16

17

18 * The correspondence should be addressed to:

19 Sheng H., Wang, Neuroscience Center, University of Helsinki

20 wang.sheng.h@gmail.com

21 or

22 J. Matias Palva, Neuroscience Center, University of Helsinki

23 matias.palva@helsinki.fi

24 **Abstract**

25 Inter-areal functional connectivity (FC), neuronal synchronization in particular, is thought to constitute a key
26 systems-level mechanism for coordination of neuronal processing and communication between brain regions.
27 Evidence to support this hypothesis has been gained largely using invasive electrophysiological approaches. In
28 humans, neuronal activity can be non-invasively recorded only with magneto- and electroencephalography
29 (MEG/EEG), which have been used to assess FC networks with high temporal resolution and whole-scalp
30 coverage. However, even in source-reconstructed MEG/EEG data, signal mixing, or “source leakage”, is a
31 significant confounder for FC analyses and network localization.

32 Signal mixing leads to two distinct kinds of false-positive observations: artificial interactions (AI) caused
33 directly by mixing and spurious interactions (SI) arising indirectly from the spread of signals from true
34 interacting sources to nearby false loci. To date, several interaction metrics have been developed to solve the
35 AI problem, but the SI problem has remained largely intractable in MEG/EEG all-to-all source connectivity
36 studies. Here, we advance a novel approach for correcting SIs in FC analyses using source-reconstructed
37 MEG/EEG data.

38 Our approach is to bundle observed FC connections into hyperedges by their adjacency in signal mixing.
39 Using realistic simulations, we show here that bundling yields hyperedges with good separability of true
40 positives and little loss in the true positive rate. Hyperedge bundling thus significantly decreases graph noise
41 by minimizing the false-positive to true-positive ratio. Finally, we demonstrate the advantage of edge bundling
42 in the visualization of large-scale cortical networks with real MEG data. We propose that hypergraphs yielded
43 by bundling represent well the set of true cortical interactions that are detectable and dissociable in MEG/EEG
44 connectivity analysis.

45

46 **Keywords** Signal leakage, spurious correlation, artificial correlation, volume conduction,
47 signal mixing, point spread, graph theory, MEG, EEG

48

49 **Highlights**

- 50 • A true interaction often is “ghosted” into a multitude of spurious edges (SI)
- 51 • Effective in controlling and illustrating SI
- 52 • Hyperedges have much improved TPR and graph quality
- 53 • Advantages in visualizing connectivity

54 1 Introduction

55 Large-scale neuronal networks, *e.g.*, manifested by functional, directed, and effective connectivity (Karl
56 J. 2011), are thought to be critical for healthy brain functions while their abnormalities are thought to underlie
57 many brain diseases (Brookes et al., 2016; Bullmore and Sporns 2009; Bullmore and Sporns 2012; Fornito et
58 al., 2015; Papo et al., 2014; Petersen and Sporns 2015; Rubinov 2015; Sporns 2014; Uhlhaas and Singer 2010;
59 Uhlhaas and Singer 2006). Currently, magneto- and electro-encephalography (MEG/EEG) are the only non-
60 invasive electrophysiological tools for studying connectivity networks with millisecond-range temporal
61 resolution and good coverage of the cortical surface (Kujala et al., 2008; Palva and Palva 2012; S. Baillet et al.,
62 2001; Salmelin and Baillet 2009). Accurately identifying interaction dynamics from MEG/EEG data is of
63 crucial importance for understanding their role in human cognition and its deficits.

64 To date, numerous interaction metrics have been developed and utilized to assess functional connectivity (FC)
65 in terms of amplitude-, phase-, and phase-amplitude correlations within or across frequency bands for pairs of
66 electrophysiological signals (Bastos and Schoffelen 2016; Kreuz 2011; O'Neill et al., 2015). These pairwise
67 metrics are typically applied to estimate FC among all brain regions, *i.e.*, to obtain “all-to-all” FC connectomes
68 (Sporns et al., 2005). Networks of inter-areal FC are often represented as graphs where brain areas constitute
69 the *nodes* (or vertices) and observed inter-areal connections the *edges* (Bullmore and Sporns 2009; Rubinov
70 and Sporns 2010).

71 FC graphs estimated from MEG/EEG sensor space data are neuroanatomically uninformative and severely
72 confounded by signal mixing. Signal mixing has two facets: first, any focal neuronal signal is picked up by
73 several sensors. Conversely, one sensor detects a mixture of signals from several distinct sources. Source
74 reconstruction can be used to reduce signal mixing and, importantly, elucidate the likely neuroanatomical
75 sources of the MEG/EEG signals (Buzsaki et al., 2012; Gross et al., 2013; Hamalainen et al., 1993; Palva and
76 Palva 2012; Schoffelen and Gross 2009). Yet, because of ill-posed nature of the inverse problem, no source
77 reconstruction approach can yield an unambiguous estimate of the source topography. Residual signal mixing
78 in source space, signal leakage, is quantitatively dependent on the source-reconstruction method of choice but
79 qualitatively characteristic to all such methods.

80 Because of signal leakage, FC measures exhibit two distinct types of false positive observations: *artificial*
81 *interactions* (AI) and *spurious interactions* (SI) (see Box 2, (Palva and Palva 2012)). AIs arise directly from
82 the signal mixing by one true signal being smeared to multiple sensors or sources, regardless of whether true
83 interactions are present. SIs are “ghost” interactions caused by the leakage of the signals from two true
84 connected nodes to their surroundings nodes that in turn become falsely connected like the truly connected
85 nodes. AIs can be suppressed by a number of bivariate metrics that typically aim to remove linear coupling
86 terms, and therefore removing artificial and true interactions with zero- and anti-phase-lag coupling. However,
87 the problem of SIs is much less acknowledged and more difficult to solve because SIs stem from multivariate
88 mixing effects. With typical distributed source modeling approaches, signal leakage causes a large number of
89 SIs that render both the network localization and graph property estimates inaccurate (Drakesmith et al., 2015).

90 To date, one solution has been proposed for correcting SIs in oscillation amplitude correlation estimates,
91 which simultaneously orthogonalizes all source time series through the Löwdin procedure (Colclough et al.,
92 2015; Colclough et al., 2016). Despite this promising advance, no solutions have yet been advanced to
93 suppress SIs for other interaction metrics.

94 Here we advance a novel approach, hyperedge-bundling, to alleviate the problem of SIs problem in all-
95 to-all connectivity analyses performed with any interaction metric. Instead of correcting the mixing effects in
96 source signals *per se*, the approach is based on a quantification of the extent of mixing between all sources,
97 evaluation of mixing similarity among all edges, and then clustering the edges into *hyperedge* bundles. This
98 procedure aims to yield a hypergraph where each hyperedge represents a true interaction and its spurious
99 reflections.

100 In this study, we performed a large set of connectivity simulations and realistic all-to-all MEG source
101 space analyses, in which we estimated phase synchrony as a measure of FC with an AI-insensitive metric. We
102 show that in simulated graphs, hyperedge bundling greatly decreases the number of false positives, *i.e.*, SIs.
103 We illustrated on real MEG data how bundling can support an informative visualization of FC graphs. We
104 suggest that such hypergraphs constitute accurate and unbiased representations of neuronal interactions
105 observable in MEG/EEG source space.

106 2 Theory

107 This section covers general topics as follows: signal mixing in MEG/EEG, how spurious interactions (SI)
108 arise from mixing between sources; and bundling of raw edges into hyperedges. The implementations specific
109 to this study are described in the *Methods* section. Throughout the report, we denote a FC graph estimated
110 from reconstructed source time series as raw graph $G_{raw} = (V, E)$, where brain regions are nodes $v_i \in V$ and
111 interactions between nodes are “raw” edges, $e_k = \{(v_i, v_j) \in E / v_i, v_j \in V\}$.

112 2.1 Signal mixing results in false positive artificial (AI) and spurious interactions (SI)

113 Let us consider a scenario where a true phase correlation is present between two distant (unmixed)
114 sources V_1 and V_2 (Fig 1A top). The signals from V_1 and V_2 are mixed with signals of their nearby and
115 mutually uncorrelated neighbours V_3 and V_4 . Estimating phase FC among all four nodes with the phase-
116 locking value (*PLV*) will reveal both the true edge $E(V_1, V_2)$ and false positive “short-range” AIs between the
117 nearby nodes $E(V_1, V_3)$ and $E(V_2, V_4)$, because *PLV* is inflated by mixing (thick gray edges, Fig 1A bottom).
118 However, due to leakage of the signal from V_1 and V_2 to their neighbors V_3 and V_4 , false positive “long-range”
119 SIs $E(V_3, V_4)$, $E(V_2, V_3)$, and $E(V_1, V_4)$ will also be observed (thin dashed edges). These SIs are thus only
120 indirectly caused by mixing and, unlike the zero-phase-lag AIs (see 2.2), SIs inherit the phase-lag of the true
121 interaction. Mixing-insensitive bivariate metrics such as the imaginary part of *PLV* (*iPLV*) can remove AIs but
122 do not eliminate SIs if the true coupling has non-zero phase lag.

123 2.2 Quantifying the mixing between reconstructed sources

124 Signal mixing/leakage between two sources is instantaneous and therefore always leads to inflated zero-
125 phase-lag correlations between the sources. Mixing does not vary over time or across frequency bands
126 (Brookes et al., 2012; Brookes et al., 2014; Drakesmith et al., 2013; Nolte et al., 2004; Palva and Palva 2012).

127 2.2.1 Source-reconstruction

128 Suppose we have a data matrix $X = \{x^{(1)}, x^{(2)}, \dots, x^{(n)}\} \in \mathbb{R}^{n \times t}$ representing narrow-band time series of t
129 samples from n neuronal sources. Simulating a MEG/EEG recording, X can be linearly projected to sensor-
130 space:

$$131 \quad Y = \Gamma X + \varepsilon \quad (1)$$

132 where $Y \in \mathbb{R}^{s \times t}$ represents the forward-modeled time series from s sensors ($n > s$). Here, $\Gamma \in \mathbb{R}^{s \times n}$ is the
133 forward operator (or the lead field) and $\varepsilon \in \mathbb{R}^{s \times t}$ is the model prediction error derived from measurement noise.
134 Next, Y can be projected back into the source-space, e.g., by minimum-norm estimation (MNE) based inverse
135 modeling:

$$136 \quad \hat{X} = WY = R\Gamma^T(\Gamma R\Gamma^T + \lambda^2\chi)^{-1}Y \quad (2)$$

137 where $W \in \mathbb{R}^{n \times s}$ is the inverse operator (sources \times sensors), λ^2 is a regularization parameter, R is the
138 source covariance matrix, and χ is the noise covariance matrix. Usually, source vertices are then collapsed onto
139 a number (50-400) of cortical parcels.

140 2.2.2 Cross-talk function and resolution matrix

141 In MEG/EEG source connectivity studies, a resolution matrix $R = W\Gamma$ ($R \in \mathbb{R}^{n \times n}$) is often used to
142 describe the relationship between true signals and modeled signals from n sources in the absence of noise
143 (Farahibozorg et al., ; Hauk and Stenroos 2014; Hauk et al., 2011; Liu et al., 2002). In R , each diagonal
144 element quantifies the sensitivity for estimating signals from that source. Each row of R is the “cross-talk”
145 function (CTF) that describes the amount of mixing between one source and all other sources. Each column of
146 R is a “point-spread” function (PSFs) that describes how the modeled signal from any one source is spread
147 across all other sources.

148 2.2.3 The mixing function

149 We approximate R numerically by a *mixing function* f_{mix} that describes the mixing between
150 reconstructed sources. We rationalize that if the true source signals are uncorrelated, the amount of correlation
151 at zero-lag between reconstructed signals can only be explained by mixing between the sources. Thus, f_{mix} can
152 be quantified by the zero-lag correlation between parcel time series estimated using a simulated MEG/EEG
153 measurement of uncorrelated source noise.

154 We first generate uncorrelated signals $X(t) \in \mathbb{R}^{n \times t}$, t samples for n parcels, and forward transform them to
155 obtain sensor signals Y (eq. 1). We next inverse transform Y to obtain \hat{X} (eq. 2). In this process, the

156 reconstructed signals $\hat{X}_0^{vi}, \hat{X}_0^{vj}$ of any two nearby sources v_i and v_j become correlated to a certain degree due to
 157 mixing. Thus, the mixing from the *true* signal of v_i to the *reconstructed* signal of v_j can be quantified as:

$$158 \quad f_{mix}(v_i, v_j) = \left| \operatorname{re}(cPLV(X_0^{(vi)}, \hat{X}_0^{(vj)})) \right| \quad (3)$$

159 where $\operatorname{re}()$ denotes the real part of a complex number and $cPLV$ is the complex-valued phase locking
 160 value:

$$161 \quad cPLV(A, B) = \frac{1}{T} \sum_{t=1}^T [e^{i(\theta_A(t) - \theta_B(t))}] = \frac{1}{T} \sum_{t=1}^T \left[\frac{S_A S_B^*}{|S_A| |S_B|} \right] \quad , \quad (4)$$

162 where T denotes the number of samples, θ_A and θ_B are the instantaneous phases of signal A and B ; S_A and
 163 S_B are complex-valued narrow-band signals from A and B , and $*$ is complex conjugate. Because mixing is
 164 instantaneous, $\operatorname{re}(cPLV(A, B))$ captures all correlations caused by mixing. For parcel pairs that do not become
 165 correlated by signal mixing, f_{mix} is near zero. For parcel pairs influenced by signal mixing, $f_{mix} \gg 0$ and
 166 reaches 1 for complete mixing.

167 **2.3 Signal mixing smears a true interaction into multiple spurious interactions**

168 For a simplified illustration of how signal mixing / source leakage produces SIs, we used model with a
 169 13×13 grid of point sources. The mixing function f_{mix} (169×169) was defined so that mixing between any
 170 two sources was a 2D Gaussian distribution decreasing with distance between the two sources (inset, Fig 1B,
 171 methods see *Supplementary*).

172 We simulated one true edge by setting two sources V_1 and V_2 to have perfect phase coupling with non-
 173 zero phase lag and keeping the remaining 167 sources uncorrelated. Next, we introduced mixing between
 174 reconstructed sources and mapped all-to-all phase FC with an AI-free metric, the imaginary part of the phase-
 175 locking-value ($iPLV$) (Palva and Palva 2012)

$$176 \quad iPLV = |\operatorname{im}(cPLV)| \quad , \quad (5)$$

177 where $\operatorname{im}()$ denotes the imaginary part of a complex number. The $iPLV$, like the imaginary coherency
 178 (Nolte et al., 2004), removes zero-lag couplings by excluding the real part of $cPLV$. Therefore, $iPLV$ yields
 179 only the true phase-lagged interactions and their false positive ghosts (SIs). In this simulation, visualization of
 180 the strongest 0.1% of $iPLV$ edges revealed the true edge and several SIs, all of which connected sources within
 181 the mixing neighbourhoods of the true sources V_1 and V_2 (Fig 1B).

182 **2.4 Raw edges can be bundled into hyperedge by their mixing similarity (S_E)**

183 The *mixing similarity* can next be derived with the known f_{mix} to describe how close these edges are with
 184 each other in signal mixing. A bivariate similarity estimation yields a mixing similarity matrix S_E , where each
 185 element $S_E(i, j)$ quantifies the similarity between two edges E_i, E_j (for how-to, see 2.5).

186 Our objective is to classify raw edges by mixing similarity into “hyperedges”, where each hyperedge is
 187 a “bundle” of raw edges (including true and SI edges): $e_k^H = \{ \{e_k = (v_i, v_j)\} \in E / v_i, v_j \in V \}$. The raw graph is
 188 thereby transformed into a hypergraph $G_h = (V, E^H)$. Within any one hyperedge, all raw edges are mixing-wise

189 close to each other but distant from the raw edges of other hyperedges, and thus collectively representing a
190 “community” of raw edges that we hypothesize to include the underlying true interaction and its ghosting SIs.

191 This classification can be done by partitioning the S_E matrix into clusters with an appropriate clustering
192 method (Fig 1C). In the simplified 13×13 toy model, bundling transformed the raw graph with a multitude of
193 false positives into a hypergraph with one hyperedge that captured the true interaction with zero false positives.

194 For visualizing hyperedges, we utilized a “force directed edge bundling” method that both indicates the
195 adjacency of the constituent raw edges and illustrates the loci where the SIs originated (Holten and Wijk 2009).

196 2.5 Hyperedge bundling for multiple true interactions

197 To demonstrate that bundling could be extended to separate multiple true interactions, we expanded the
198 simulation and modeled interactions with three degrees of adjacency: “kin”, “nearby”, and “far”. The
199 estimated raw graph yielded the true-positive (TP) edges surrounded by numerous false positive (FP) SIs (Fig
200 2D). Estimating and partitioning the edge similarity matrix S_E revealed that: 1) two “kin” edges were
201 inseparable and together with their SIs they merged into the largest hyperedge HE_1 (Fig 2E); 2) the “far” pair
202 was clustered into two clearly separable hyperedges HE_2 and HE_5 ; 3) the “nearby” pair and their SIs were also
203 clustered into two distinct hyperedges HE_3 and HE_4 with greater inter-hyperedge similarity as measured by
204 mean-linkage (green box) than the “far” pair (magenta box); 4) a few scattered random false positive edges
205 were also clustered into hyperedges (gray box), but they were much smaller in size than any of the hyperedges
206 containing a true edge.

207 If a hyperedge containing at least one true raw edge is considered as a TP observation, bundling greatly
208 decreased graph noise in terms of the FP/TP ratio. FP/TP in raw graph was 239/6 and 4/5 in the hypergraph,
209 which marks a reduction in the fraction of FPs by a factor of 50. Visualizing these bundles showed that the
210 hypergraph had less visual clutter and facilitated identification of the true interactions compared to the raw
211 graph (Fig 2F).

212 2.6 Estimation of the edge similarity matrix S_E

213 Hyperedge bundling is based on the raw connectivity graph A_{FC} (a sparse matrix containing only
214 significant edges), and the mixing function f_{mix} (Fig 2A, C). We first parsed the edges in A_{FC} into a list of node
215 pairs (Fig 2B). We next find the mixing between all the involved nodes from f_{mix} (Fig 2C, and colour-coded
216 and illustrated geometrically in Fig 2D) to compute the edge-to-edge adjacency in signal mixing.

217 2.6.1 The edge adjacency matrix (A_E)

218 For a raw graph with m edges, the edge-to-edge adjacency matrix $A_E \in \mathbb{R}^{m \times m}$ represents the pairwise
219 mixing adjacency among all raw edges and is necessary for computing the similarity matrix S_E . The adjacency
220 between two edges $E_i(V_1, V_2)$ and $E_j(V_3, V_4)$ was defined as follows (Fig 2D):

221 if $V_1 \sim V_4$ are distinct nodes

$$222 A_E(i, j) = \max [f_{mix}(V_1, V_3) f_{mix}(V_2, V_4), f_{mix}(V_1, V_4) f_{mix}(V_2, V_3)]$$

$$223 \text{elseif } V_1 = V_3 : A_E(i, j) = f_{mix}(V_2, V_4)^2$$

224 *elseif* $V_2 == V_4 : A_E(i,j) = f_{mix}(V_1, V_3)^2$
 225 *elseif* $V_1 == V_4 : A_E(i,j) = f_{mix}(V_2, V_3)^2$
 226 *elseif* $V_2 == V_3 : A_E(i,j) = f_{mix}(V_1, V_4)^2$
 227 *elseif* $i == j : A_E(i,j) = 0$ % diagonal of A_E (6)

228 here “==” is assertion, “=” is assignment. This algorithm is applied for all pairs of edges in the raw
 229 graph to populate the A_E matrix (Fig 2E).

230 **2.6.2 Evaluation of Edge Similarity (S_E) with correlation of edge mixing profiles in A_E**

231 We denote rows of the A_E matrix as the *signal mixing profiles* so that $A_E(i)$ and $A_E(j)$ are the mixing
 232 profiles of edges E_i and E_j , respectively, and thus indicate their mixing adjacency to all the other raw edges in
 233 the graph. If E_i and E_j are similar to each other, *i.e.*, a high correlation between $A_E(i)$ and $A_E(j)$, edge E_i will be
 234 similar to all the edges in the raw graph that E_j is similar to, and vice versa (Fig 2F&2G). Such pattern can be
 235 already observed in the simplified models (Fig1) where SIs of any given true edge are all close to each other
 236 and adjacent to the true interaction.

237 Conversely, if two edges are far apart in mixing, their mixing profiles exhibit little to no correlation.
 238 Using correlation estimates of mixing profiles, it is thus possible to assess the significant similarity of all pairs
 239 of edges in A_E and populate the similarity matrix $S_E \in \mathbb{R}^{m \times m}$ (Fig 2H). The significance level of the correlation
 240 can be determined through a Fisher z-transformation. Hyperedge bundling is based on the notion that a S_E can
 241 be partitioned into clusters of raw edges that are similar to each other in mixing within each cluster and
 242 therefore to collectively reflect a shared true underlying interaction.

243 **2.7 The resolution of hyperedge bundling is defined by the cutoff limit**

244 We partition the edge similarity matrix S_E into clusters of “hyperedges” so that within any one
 245 hyperedge, the raw edges are mixing-wise close (large S_E values) to each other and distant (small S_E values)
 246 from raw edges of other hyperedges.

247 We now introduce a control parameter, the *cutoff limit* (CL) that dictates the “resolution” of a
 248 hypergraph. CL is defined as the ratio of desired number of clusters to the number of available raw edges to be
 249 clustered. For example, for a graph of 1000 edges, a CL of 0.1 causes the clustering method to partition the S_E
 250 matrix into 100 hyperedges. We chose to control clustering using the CL for better comparability of clustering
 251 methods or graphs of different sizes. The similarity matrix $S_E \in \mathbb{R}^{m \times m}$ can be partitioned into arbitrary number
 252 of clusters from 1 to $m - 1$, *i.e.*, CL ranging from $1/m$ to $(m-1)/m$ (Fig 2I, for details, see *Supplementary*).

253 **2.8 Validate the stability of hyperedge clustering**

254 To ensure that the hyperedges are not random outcomes of partitioning the similarity matrix, the
 255 “stability” of partitioning solutions must be evaluated. We ask, at any resolution (CL=c), if the differences
 256 between the partitioning solutions of n randomly perturbed versions of a similarity matrix S_E is statistically
 257 smaller than their surrogate counterparts, the partitioning solution can be considered as stable (*Supplementary*).
 258 The distance between two partitioning solution can be estimated with the *variation of information* (VI, (Meilă

259 2007)). The independent perturbations to a similarity matrix can be acquired by randomly deleting a small
260 subset, *e.g.*, 10~20%, of the elements in the similarity matrix (Ben-Hur et al., 2002; Williams et al., 2015). The
261 surrogates can be obtained by randomly rewiring the original similarity matrix.

262 **3 Methods**

263 The goal of this study was to assess the performance and applicability of hyperedge bundling in
264 suppressing spurious interactions (SI) in MEG/EEG source connectivity studies. To this end, we obtained
265 large numbers of functional connectivity (FC) graph estimates from simulated data with realistic sources and
266 inverse modeling. We next evaluated the efficacy of hyperedge bundling in capturing true positive (TP)
267 interactions and rejecting false positive (FP) SIs. Finally, we demonstrated the bundling of FC graphs
268 estimated from MEG data recorded in a visual working memory (VWM) experiment.

269 This section includes the procedural outlines of the simulations and evaluation of bundling efficacy. The
270 preprocessing pipeline, technical details of the simulations and preprocessing of the VWM experiment are
271 described in *Supplementary*.

272 **3.1 Simulating “truth” time series of varying coupling strengths**

273 In real electrophysiological data, mixing is inhomogeneous across source loci and subjects (Brookes et
274 al., 2014) and coupling strengths of neuronal interactions also exhibit great spatiotemporal and inter-subject
275 variability (Preti et al., 2016; Zalesky et al., 2014). To account for such variability, we created 1000 distinct
276 *truth* graphs each containing 200 randomly generated true interactions between 400 cortical parcels in a
277 standard cortical source space. Each node thus connected only to a single other node, which allows an
278 unbiased survey of the whole cortical surface in every graph realization. We did not simulate structured
279 networks to exclude the impact of higher order SI here. These higher order SI can arise from common drive,
280 third-party sources, and cascade effects, although identifying them is of equal importance (Mannino and
281 Bressler 2015; Wollstadt et al., 2015).

282 For every truth graph, we simulated ten sets of time series, representing two different modes of coupling
283 (gamma distribution or uniform distribution) at 5 different levels of coupling strength each (Supplementary).
284 A set of uncorrelated time series was also simulated as null hypothesis H_0 for each truth graph which would be
285 used for estimating the source-space mixing properties and as the baseline condition in group analysis.

286 **3.2 Estimation of mixing properties using the H_0 time series**

287 Mixing in source reconstructed MEG/EEG data is essentially captured in the forward and inverse
288 operators used in source reconstruction. These operators are determined by the data acquisition system and
289 specifics of the individual source model (Wens 2015). In addition to the mixing function f_{mix} (see 2.2.3), we
290 characterized the source model used here with a set of additional mixing metrics obtained from the 12 subjects
291 from the VWM experiment:

292 1) Parcel fidelity, f_p , that quantifies the reconstruction accuracy and is defined as the phase correlation
293 between the simulated H_0 , and reconstructed \hat{H}_0 , time series of each parcel v_i

$$294 \quad f_p(v) = \left| \text{re}(cPLV(x_0^{(vi)}, \hat{x}_0^{(vi)})) \right|. \quad (7)$$

295 2) Edge fidelity, $f_e(v_i, v_j) = f_p(v_i)f_p(v_j)$, that indexes the reconstruction accuracy of raw edges connecting
296 nodes v_i and v_j .

297 3) Residual spread function, $PLV_0(v_i, v_j)$, that is the phase correlation between two parcels' reconstructed
298 (\hat{H}_0) time series.

$$299 \quad PLV_0(v_i, v_j) = \left| \text{re}(cPLV(\hat{x}_0^{(vi)}, \hat{x}_0^{(vj)})) \right| \quad (8)$$

300 The definition of PLV_0 appears similar to that of f_{mix} , but they are conceptually different. The f_{mix}
301 measures how much of each source's true signals are picked up in other sources' reconstructed signals. PLV_0 ,
302 on the other hand, is the correlation between any two sources' modeled \hat{H}_0 time series where both are
303 contaminated by mixing with numerous other sources. Because the $iPLV$ estimates can be biased by mixing,
304 we used PLV_0 to exclude edges connecting sources with large mixing.

305 **3.3 Elimination of poorly measurable edges with the intractable-edge-mask (IEM)**

306 We applied an intractable-edge-mask (*IEM*) to exclude edges that connect sources with poor
307 reconstruction accuracy. True interactions between these sources may exist, but cannot be reliably detected
308 because estimations of connectivity between them are unreliable due to the limitations of the source model.
309 We utilized the mixing properties (see 3.2) and construct a group-level *IEM* in two steps:

- 310 1) With average edge-fidelity $\langle f_e \rangle$ and the residual spread $\langle PLV_0 \rangle$, we create two Boolean masks:
 - 311 i. The edge-fidelity mask (M_{f_e}) to exclude edges with low fidelity, thereby removing edges
312 connecting poorly reconstructed sources.
 - 313 ii. The residual spread mask (M_{PLV_0}) to exclude edges with large PLV_0 , thereby removing edges
314 whose FC estimates likely are much distorted by mixing between these loci.
- 315 2) The *IEM* is the union of these two masks.

316 In this study, we set 0.1 as the threshold for M_{f_e} , which removed the 40% most poorly reconstructed
317 edges from all 79,800 ($N(N-1)/2$, $N = 400$) possible edges in raw graphs. The M_{PLV_0} was acquired by deleting
318 edges whose PLV_0 was greater than the 95th percentile of the PLV_0 matrix.

319 **3.4 Estimation of group-level FC of simulated graphs**

320 The group-level significant $iPLV$ estimates thresholded with the *IEM* were used as raw graphs for
321 hyperedge bundling. The group-level analysis for the simulated graphs and for real MEG/EEG data in the
322 VWM experiment were carried out in the same manner. For simulated graphs, we forward- and inverse-
323 modeled the coupled truth time series into 12 subjects' individual source space, thereby introducing mixing
324 into reconstructed signals (Schoffelen and Gross 2009). We next estimated $iPLV$ connectivity for these
325 subjects. We then tested across subjects, for each edge in every estimated FC graph, whether there was a

326 significant difference (one-tailed t-test) in the *iPLV* estimate between the coupled and the H_0 condition. Those
327 edges that showed a significant difference were identified as raw edges (corrected for multiple comparisons
328 within each FC graph). We acquired FC graphs with three significance levels $p < 0.05$, 0.01 , and 0.001 for
329 each of the ten coupled time series.

330 **3.5 Hyperedge bundling with two clustering methods**

331 After applying the *IEM* to all group-level FC matrices, we followed the procedures described in *Theory*
332 to obtain the similarity matrix S_E for each FC. We next partitioned each S_E into clusters of “hyperedges” with
333 two clustering methods. The unweighted pair group method with arithmetic mean (UPGMA) is an
334 agglomerative hierarchical clustering method that builds a rooted hierarchical tree to represent the distance in
335 signal mixing between all raw edges (Jain et al., 1999). The Louvain method for community detection extracts
336 communities by optimizing the modularity of clusters through a gradient descent procedure (Blondel et al.,
337 2008)(Blondel et al., 2008).

338 **3.6 Comparing hypergraphs with raw graphs**

339 We denoted the TPs as the edges from truth graphs that were identified as significant edges in the
340 group-level FC matrix, and FPs as significant edges in the group-level FC matrix but absent in the truth graph.
341 Thus, the true positive rate (TPR, sensitivity) is given by $TPR = TP/N_{true*}$, where N_{true*} is the number of
342 “detectable true edges” referring to the number of simulated true edge that passed the intractable-edge-mask.
343 We further defined the *noise* as the FP to TP ratio. An ideal group-level FC should capture as many of the true
344 interactions as possible while rejecting other edges, *i.e.*, high TPR and low FP/TP.

345 We used TPR and FP/TP as the main criteria to characterize raw graphs instead of the commonly used
346 receiver operating characteristic curve (ROC) for two reasons. First, the ROC is derived from the TPR and
347 false positive rate (FPR) which are not directly comparable between raw graphs and hypergraphs, as these are
348 different constructs; second, because the number of FP is disproportionally larger than that of TP (as shown
349 later with an example), the shape of the ROC is misleadingly optimal when limiting the number of raw edges
350 with varying edge weight threshold.

351 We defined a TP hyperedge (TP_{HE}) as a hyperedge capturing at least one TP raw edge, whereas a FP
352 hyperedge (FP_{HE}) contained only FP raw edges. Hyperedges may also contain multiple TP raw edges. To
353 quantify this, we defined *separability* as the fraction of true positive hyperedges that contain only one TP raw
354 edge out of all true positive hyperedges. An ideal hypergraph should balance high TPR and separability
355 against low FP/TP.

356 **4 Results**

357 This section includes three parts: 1) Demographics of group-level FC of the simulated graphs; 2) Efficacy
358 of hyperedge bundling; 3) Application of hyperedge bundling to real MEG data.

359 4.1 Group-level FC as raw graphs

360 In individual subjects, mixing introduced by the virtual MEG experiment distorted PLV , $iPLV$ and the
361 phase-lag of all measured graphs of varying coupling strength including the H_0 time series (*Supplementary*).
362 To find group-level significant edges, we tested for each edge whether there was a difference in $iPLV$ value
363 between the coupled condition and the H_0 condition (Fig 3A, see 3.4). Edges that showed a significant
364 difference were reported as raw edges (corrected for multiple comparisons). Thus, we obtained FC graphs for
365 each of the ten sets of coupled graphs at 3 significance levels of $p < 0.05$, 0.01 and 0.001.

366 4.1.1 Raw graphs of $iPLV$ edges are noisy

367 Overall, the number of significant $iPLV$ edges increased as coupling strengths increased (Fig 3B). The
368 group-level graphs at all 3 significance levels captured over 75% of all detectable TP edges, except in the case
369 of weak uniform coupling, $C_c(0.1)$ (Fig 3C). We simulated 200 random edges in each ground truth graph and
370 computed the true positive rate (TPR) for each measured group graph as the number of significant edges
371 divided by the number of all simulated true edges that passed through the intractable-edge-mask (IEM).
372 Despite the high TPR, there was a large variability in the ratio of false and true positives, FP/TP, across these
373 graphs (Fig 3D).

374 4.1.2 Is strict statistical thresholding a good solution for pruning FPs?

375 We chose the graphs of gamma coupling $C_\gamma(r=15)$ and uniform coupling $C_c(0.5)$ to test statistical
376 thresholding (below) and hyperedge bundling (4.2) because they had comparable TPR (Fig 3C) and equivalent
377 true edge strengths (see distribution in *Supplementary 1*). Moreover, both contained only ~750 edges, which
378 mitigated computational overhead in later clustering analyses.

379 One sensible way to identify key structures in FC graphs is to apply a statistical threshold to $iPLV$
380 values. We found that by increasing the significance $iPLV$ threshold, the number of FP edges decreased at a
381 faster rate than the number of TP edges in both graphs (Fig 3E). Around 120 of the 640 strongest edges were
382 TP, giving a TPR > 90% for 125 detectable true edges, but a FP/TP ratio of 4. When retaining the 20 strongest
383 edges reduced the FP/TP to 0.1 (Fig 3F) but at the cost of reduced TPR, (TPR = 0.15). Overall we found that
384 the mean $iPLV$ of TP edges was larger than that of FP edges' (Fig 3G), which suggests that strict thresholding
385 is an applicable solution for reducing FP/TP but comes at a price of an elevated false negative rate, although
386 the shape of ROC curve appeared to be optimal (inset Fig 3E).

387 4.2 Hypergraphs yields better FP/TP than raw graphs with reasonable TPR cost

388 4.2.1 The stability of clusters

389 Evaluating the stability of clustering was a necessary step prior to further analysis of the properties of
390 hyperedge clusters. The resolution of clustering and thereby of the hypergraphs was controlled by the *cutoff*
391 *limit* (CL, see 2.6). We used bootstrapping to identify the CL range that yielded stable partitioning of the raw
392 graphs (see *Methods* and *Supplementary*). We found that at $CL < 0.4$, both UPGMA and Louvain clustering

393 yielded significantly more stable partitions for simulated graphs than their randomly rewired counterparts (Fig
394 4A). For the 640 raw edge graphs, this CL upper bound corresponded to ~250 hyperedges. In the following
395 analysis, we thus tested bundling with CL ranging from 0.05 to 0.45.

396 4.2.2 Cluster-size distribution

397 We next quantified the distributions of hyperedge sizes (numbers of raw edges per hyperedge, Fig 4B)
398 by pooling hyperedges from 500 clustered graphs with CL ranging from 0.05 to 0.45. As expected, we found a
399 systematic shift towards smaller hyperedges with increasing resolution/CL. The Louvain method consistently
400 yielded more small hyperedges than UPGMA.

401 4.2.3 Hyperedge-bundling performance: trade-offs between separability, TPR and graph noise

402 Hyperedge bundling aims to detect and separate as many TP interactions as possible while rejecting as
403 many FP as possible. We tried to find an optimal balance among these competing outcomes by taking into
404 account two aspects of hyperedge bundling: separability and noise. We defined *separability* as the ratio
405 between singleton TP hyperedges (containing only one TP raw edge) and all TP hyperedges, and *noise* as the
406 FP/TP ratio of the hyperedges. An ideal hyperedge partitioning would thus have *separability* = 1, FP/TP ~0,
407 and a TPR equal to the TPR of raw edges.

408 We observed that by increasing the hyperedge resolution (CL from 0.05 to 0.45), the *separability*
409 increased but noise also increased with both clustering methods (Fig 4C, 4D). Thus at coarse resolutions (low
410 CL), multiple TP raw edges were partitioned into one hyperedge but there were very few FP hyperedges,
411 likely because there were less small-sized hyperedges. Conversely, at fine resolutions (high CL), separability
412 was improved but at the cost of having greater numbers of FPs.

413 Knowing that small hyperedges are more likely to be FPs than large hyperedges (Fig 1E), we further
414 tested whether excluding hyperedges by size would decrease noise. At each resolution level, excluding small
415 hyperedges lead to a decrease in noise (FP/TP decreased with increasing θ_{HEsize} , Fig 4C, D). Nevertheless, this
416 was accompanied by reduced separability (y axis, Fig 4C, D) and a reduced TPR (Fig 4E, F) caused by the
417 removal of small-sized TP hyperedges together with FP hyperedges.

418 To summarize, at all graph resolutions, hypergraphs were less noisy than raw edge graphs. In the least
419 noisy hypergraph (*e.g.*, Louvain, CL = 0.05 and $\theta_{HEsize} > 8$), 87% of the 125 TP raw edges were retained while
420 achieving a 10^3 -fold decrease in noise compared to the underlying raw graphs, *i.e.*, FP/TP decreased from
421 $(640-125)/125 = 4.1$ (C_γ raw graphs in Fig3E) to 3.8×10^{-3} (leftmost filled box on the cyan curve, Fig 4F).
422 Nevertheless, this improvement came at the cost of poor separability, meaning many hyperedges in CL = 0.05
423 graphs contained several true edges. To balance an optimal trade-off, we decided to use $CL \geq 0.15$ and $\theta_{HEsize} >$
424 2, expecting to achieve a reduction of FP/TP to 0.1 (from 4.1 in raw edges) with negligible reduction in TPR
425 and adequate separability (0.5).

426 **4.2.4 Louvain clustering yields less noisy hypergraphs but lower separability than UPGMA clustering**

427 The Louvain method produced more small hyperedges than the UPGMA method (Fig 4B). Although the
428 Louvain hypergraphs had higher level of noise when retaining singleton hyperedges ($\theta_{HEsize} = 0$), this relation
429 was inverted when singleton hyperedges were screened (Fig 5A). This indicates that the majority of the
430 singleton hyperedges yielded by Louvain were FPs. Moreover, the Louvain hypergraphs had greater TPR
431 when CL values were between 0.15 and 0.25 (Fig 5B). These advantages, however, came at the cost of
432 separability, which was better with UPGMA throughout the tested range (Fig 5C).

433 **4.3 Visual working memory networks: real MEG data**

434 To assess the feasibility of using hyperedge bundling with real MEG/EEG data, we applied bundling to
435 raw graphs that reflected significant strengthening of inter-areal phase synchronization during memory
436 retention compared to pre-stimulus baseline during a visual working memory task (see *Supplementary* and
437 Honkanen et al., 2015).

438 We found that the *iPLV* estimates in alpha- and gamma-frequency band were greater during memory
439 retention than in pre-stimulus baseline. Here, we picked the 1000 strongest *iPLV* edges and drew them as lines
440 linking the synchronized parcels on a flattened cortical surface (Fig 6A, 6B). We also illustrated a randomly
441 picked graph from our simulations as a comparison (Fig 6C). We applied hyperedge bundling (UPGMA with
442 $CL=0.15$, $\theta_{HEsize}>6$) to these raw graphs. The resulting hypergraphs, the real MEG and simulated FC graphs
443 alike, offer better visualization of large-scale FC than raw graphs, emphasizing the long-range
444 synchronizations between brain regions(Fig 6D, 6E, 6F).

445 **5 Discussion**

446 MEG and EEG have great potential for yielding insight into the spatio-temporal structure of brain
447 connectivity. Nonetheless, due to the ill-posed nature of the inverse problem, linear mixing and inaccurate
448 source localization complicate MEG/EEG connectivity analyses both by distorting phase and amplitude
449 estimates and by leading to false positive observations of artificial (AIs) and spurious interactions (SIs). We
450 advance here a novel methodological framework, hyperedge bundling, to suppress SIs in brain connectivity
451 graphs. We found that hyperedge bundling can be used to reduce the false positive rate with moderate to little
452 decrease on the true positive rate.

453 Hyperedge bundling has several features that are advantageous and facilitate its application. First, since
454 it is done only after interaction analyses, it does not require sophisticated preprocessing to suppress mixing
455 effects in the original source time series. Hyperedge bundling only requires the forward and inverse operators
456 and a mixing function estimated analytically or from simulations. Accordingly, it also inherently takes the
457 source-model heterogeneity appropriately into account. Hyperedge bundling is also independent of the
458 interaction metric and can be applied to connectomes estimated with any bivariate interaction metric. Finally,
459 the nodal groups in the hypergraph obtained from hyperedge bundling constitute data-driven coarsening of
460 originally high-resolution source parcellations. We suggest that these nodal groups be more representative of

461 the true co-active local areas than *a priori* constructed low-resolution parcellations. This can be an aspect for
462 future work.

463 In summary, hyperedge bundling can be used to suppress SIs and identify putative true edges in brain
464 connectivity data and thereby to improve the localization of true interacting neuronal networks.

465 ***Hyperedge bundling vs. edge thresholding: reducing FP/TP while maintaining acceptable true positive rate***

466 Some connectivity studies have reduced the amount of edges by applying strict criteria on edge
467 selection. However, biases and instability of graph properties can be introduced when using arbitrary threshold
468 criteria on raw edges (Drakesmith et al., 2015; van Wijk, Bernadette C. M. et al., 2010) and weak connections
469 may also play an important role in cognitive functions (Santarnecchi et al., 2014). Nevertheless, imposing
470 strict criteria for thresholding is an attractive option for increasing the fraction of true positives among all
471 observations, *i.e.*, decreasing the FP/TP ratio (see Fig 3E and F) and for focusing the outcome on most robust
472 effects. However, this approach, while effective in excluding FPs (SIs), also excludes a large fraction of true
473 positives. For example, we found that in raw graphs when we applied a threshold strict to decrease noise
474 (FP/TP ratio dropped from 4 to 0.1), but the TPR was reduced to 0.15. In contrast, with hyperedge bundling
475 we could obtain the same noise level (FP/TP of 0.1) while preserving a TPR of up to 0.88 (see brown line, Fig
476 4F). Hyperedge bundling is thus superior to strict thresholding in attenuating FP/TP with little decrease in TPR.

477 Importantly, our simulations show that the raw edges with largest correlational estimates might not
478 correspond to the strongest or most important neurophysiological connections because these estimates appear
479 to be correlated with reconstruction accuracy (*Supplementary*). The reconstruction accuracy is heterogeneous
480 across source space, meaning high accuracy of sources may positively bias the *iPLV* estimates. This bias is
481 another reason for including weak observations in FC graphs.

482 ***Control parameters of hyperedge determine resolution and the balance among FP/TP, TPR, separability***

483 In the current implementation, hyperedge bundling is controlled by the cutoff limit (CL) and the
484 hyperedge size threshold (θ_{HEsize}). CL determines the resolution of the hypergraph and the balance between
485 noise (FP/TP) and *separability* of true hyperedges. Low CL values lead to low noise in hypergraphs but poor
486 separation of true raw edges into distinct hyperedges. θ_{HEsize} can be used to prune the smallest hyperedges to
487 further reduce noise, albeit at a cost of pruning TP hyperedges.

488 We compared two clustering methods, UPGMA and Louvain. While the results showed clearly that by
489 and large both clustering methods yielded similar performance, each method had interesting advantages.
490 Louvain yielded better TPR than UPGMA for CL values between 0.05 and 0.25 (see Fig. 5B), and lower noise
491 when singleton hyperedges were excluded (see Fig. 5A). UPGMA, on the other hand, yielded better
492 separability of TP hyperedges throughout the control parameter ranges. Overall, using either clustering method
493 with CL = 0.15–0.25 and $\theta_{HEsize} = 1$ –2 will yield a large reduction in FP/TP (from 4 to 0.1–0.2) with good
494 separability and negligible reduction in TPR.

495 In applications to real data where the truth graph is unknown, choosing parameters, *i.e.*, to control the
496 trade-off between suppressing noise and maintaining high TPR and separability, can be based on both our

497 simulation results and objectives of the research. If the objective of the hypothesis requires good separability
498 (e.g., connectivity between specific visual areas to inferior parietal region), one should create high resolution
499 hypergraphs, but this will be accompanied by sub-optimal noise reduction. Conversely, if the objective is to
500 establish connectivity between the visual and parietal regions, a low resolution hypergraph (with low noise) is
501 pertinent.

502 ***Comparison of hyperedge bundling and symmetric orthogonalization***

503 Symmetric orthogonalization is a pioneering solution to the overall problem of SIs in the context of
504 amplitude correlation estimation (Colclough et al., 2015). Its predecessor, pairwise orthogonalization (Brookes
505 et al., 2012; Hipp et al., 2012) excluded instantaneous mixing and evaluated amplitude correlations for each
506 time-series pair at a time. It is thus applicable to the estimation all-to-all amplitude correlations similarly to
507 any other bivariate AI-free metric for phase or other forms of coupling, and also suffers from SIs in the same
508 manner.

509 Symmetric orthogonalization overcomes the problem of SIs by simultaneously removing zero phase-lag
510 components from all source time series through a gradient descent procedure known as the Löwdin
511 orthogonalization (Everson 1999; Löwdin 1950). Next, all-to-all amplitude correlations are estimated with
512 partial correlation of amplitude envelopes to keep direct and remove indirect interactions (Marrelec et al.,
513 2006). Because the partial correlation matrix is expected to be sparse, a graphical lasso regularisation of the
514 inverse covariance matrix is applied to penalize near-zero elements (Banerjee et al., 2008; Friedman et al.,
515 2008), which reduces noise in the partial correlation graph.

516 Symmetric orthogonalization effectively attenuates SIs caused both by signal leakage and by indirect
517 true couplings (i.e., $A \leftrightarrow C$ correlation, when true correlations are $A \leftrightarrow B \leftrightarrow C$). The two limitations of this
518 method are: *i*) it is applicable only to the estimation of amplitude correlations, *ii*) it is limited by the rank of the
519 data due to its dependence on singular value decomposition. For MEG/EEG data that are preprocessed with
520 signal space separation (SSS) and temporal SSS methods, the rank of the data (~degrees of freedom) is often
521 limited to 60–70 (Haumann et al., 2016). Thus, symmetric orthogonalization should be applied to cortical
522 networks with less than 60–70 independent sources, such as the 19 regions per hemisphere used in (Colclough
523 et al., 2015). For studying FC with greater parcellation resolutions ($>>70$) or with interaction metrics other
524 than amplitude correlations, hyperedge bundling thus provides an alternative method for SI suppression. The
525 similarities and differences between symmetric orthogonalization and hyperedge bundling are summarized in
526 Table 1.

527 ***Optimal source space for brain connectivity analyses***

528 There are numerous source reconstruction methods for MEG/EEG and the choice of method may have
529 profound impacts on source connectivity analysis due to their difference in sensitivity to various
530 synchronization profiles of the interacting sources (Hincapié et al., 2017). Although in the present study we
531 used linear inverse operators (Hamalainen and Sarvas 1989; Hamalainen and Ilmoniemi 1994; Lin et al., 2006),

532 hyperedge bundling can also be used with other source reconstruction methods as long as the amount of
533 mixing among the sources/parcels can be quantified.

534 Parcel numbers in current MEG/EEG source connectivity studies range from tens of parcels, *e.g.*, 38 in
535 ((Colclough et al., 2015) and around 70 in (Farahibozorg et al., ; Hillebrand et al., 2012), up to 200-400
536 parcels(Lobier et al., 2017; Siebenhuhner et al., 2016; Zhigalov et al., 2017). We propose that the source-space
537 for FC studies should have a fine spatial resolution that enables the separation of nearby independent signals to
538 an extent allowed by the source reconstruction approach. Neither the neuronal source constellations nor the
539 degrees of freedom in the data are likely to match any *a priori* chosen parcellation scheme and hence coarse
540 parcellations can misrepresent or miss source areas that fall in between the parcels or are much smaller than
541 the parcels.

542 Our approach to use 400 parcels aims to eliminate the possibility of such pitfall. Moreover, with fine-
543 grained parcellations, hyperedge bundling can well measure the mixing among raw connectivity edges and
544 produce hypergraphs with high confidence of capturing and separating true interactions. Furthermore, the
545 nodal groups connecting hyperedges can be utilized to coarsen a fine-grained source space in a data-driven
546 manner and with consideration of the constraints posed by the source model. On the other hand, hyperedge
547 bundling will likely to fail in a source-space of low spatial sampling, where the mixing similarity between
548 observed edges is likely to be low due to initial low mixing among neighboring parcels.

549

550 **6 Acknowledgements**

551 We thank Prof. Karim Jerbi for comments to the work. We thank Dr. Giles Colclough for sharing source
552 code and his insights to the symmetric orthogonalization method. This research was funded by the Academy
553 of Finland grants 266745 and 281414. The funding bodies had no role in the design, data acquisition and
554 analysis, decision to publish, or preparation of the manuscript.

555 **7 Table**

	Symmetric orthogonalization (Colclough et al., 2015)	Hyperedge bundling
Type of FC	<ul style="list-style-type: none"> • Amplitude-correlation 	<ul style="list-style-type: none"> • Any form of FC or EC
Data for FC estimation *	<ul style="list-style-type: none"> • A symmetric multivariate correction is first operated on \mathbf{Z} (narrow-band amplitude-envelope time series) to obtain \mathbf{P} that is the best approximation of \mathbf{Z} in multivariate linear regression sense, and in \mathbf{P}, each source's time series is simultaneously orthogonal to each other thus zero-phase-lag free between all source-pairs. \mathbf{P}'s amplitude-envelope is next down-sampled to obtain $\tilde{\mathbf{P}}$ 	<ul style="list-style-type: none"> • Any narrow- or broad-band time series • Estimation of the mixing functions: $f_{mix}(v_i, v_j)$ and edge-fidelity $f_e(v_i, v_j)$ is a prerequisite
Procedure of FC estimation	<ul style="list-style-type: none"> • 2 steps: 1) regularize Ω (the inverse of covariance matrix of $\tilde{\mathbf{P}}$), imposing sparsity (Freidman et al., 2008) on the graph to maximise the log-likelihood of a multivariate Gaussian graph model; 2) Compute partial correlation based on the regularized Ω 	<ul style="list-style-type: none"> • 2 steps: 1) estimate pairwise FC, 2) bundle raw edges obtained in (1) using $f_{mix}(v_i, v_j)$
Advantages	<ul style="list-style-type: none"> • Effective in removing SIs • Regularized partial correlation reports direct FC between $\tilde{\mathbf{P}}$ and excludes indirect FC • Computational efficient 	<ul style="list-style-type: none"> • Requires no alteration to source-reconstructed time series • Not limited by the rank of the source time series, which allows a high spatial resolution source estimates • Hyperedge bundling can be used with any directed or undirected interaction metric
Limitations	<ul style="list-style-type: none"> • Blind to true zero-phase-lag interactions • Likely insensitive to low SNR sources • Limited by the rank of the time series • Risk of reporting false positives if the time series are non-Gaussian 	<ul style="list-style-type: none"> • Blind to true zero-phase-lag interactions dependent on the choice of the interaction metric • The resolution of the hypergraph is a free parameter

556

557

558 **Figure captions**

559 **Fig 1**

560 *Spurious edges are indirect products of mixing and they can be bundled. A)* Top: signal mixing causes
561 the detection of artificial (AI) and spurious interactions (SI). Bottom: AIs are always zero-lag connections
562 (solid gray edge) whereas SIs (dashed gray edges) are “ghosts” of the phase-lag of the true interaction (dashed
563 black edge) and thus can be either zero-lag or, more often, non-zero-lag interactions. **B)** Toy model 1: one
564 single true interaction $E(V_1, V_2)$ on a grid of 13 x 13 point sources. Inset shows the simulated mixing
565 neighbourhood of V_1 and V_2 . FC was estimated with *iPLV*, and the true edge (black) was discovered with
566 multiple SIs (grey) originating from both sources’ mixing neighbourhoods. **C)** The similarity in signal mixing
567 between all edges (true and SI) can be quantified and all these edges can be bundled into one hyperedge. **D)**
568 Toy model 2: three pairs of true edges of varying spatial distance were simulated. **E)** Partitioned similarity
569 matrix S_E , for toy model 2, where each row represents one edge and one cluster represents a hyperedge. The
570 grey box indicate false-positive hyperedges; the magenta and green boxes indicate the inter-hyperedge
571 similarity between the “far” and “nearby” pair. **F)** Visualization of the hyperedges defined in **E**.

572 **Fig 2**

573 *Bundling of raw edges into hyperedges. A)* The true interaction E_1 and one of its SIs E_2 from Fig 1B
574 schematically shown in matrix form. **B)** The raw graph A_{FC} (a sparse matrix containing only significant edges)
575 is parsed to a list node pairs, each pair representing one edge. **C)** For E_1 and E_2 , the mixing between all of their
576 constituent nodes can be found in the mixing function f_{mix} . **D)** The edge adjacency (A_E) between E_1 and E_2 is
577 the maximum product of constituent nodes’ mixing. **E)** A_E is computed for all the pairs of edges found in A_{FC} .
578 Data taken from a randomly selected simulation. **F)** Examples of edges that are similar (blue) and not similar
579 (red) in their mixing profiles. **G)** Similarity between two edges is the correlation between two edges’ mixing
580 profiles. **H)** Mixing similarity matrix S_E . **I)** The partitioning of this S_E at low, medium and high resolutions.

581 **Fig 3**

582 *The demographics of group-level FC of simulated graphs A)* Significant edges were determined with a
583 paired one-tailed t-test between a coupled-edge condition (k1) and the H_0 condition for simulated graphs. **B)**
584 For initial evaluation of bundling, we chose one set of gamma-distribution-coupled (C_γ) and one set of
585 uniform-distribution-coupled (C_c) graphs, which are indicated by the markers. **C)** True positive rate TPR (see
586 methods) of the two chosen graphs was above 90%. **D)** The true positive rate (TRP) as a function of noise
587 (FP/TP) for all coupling strengths. **E)** In the chosen sets of graphs, the number of FP decreases exponentially,
588 while the number of TP decreases linearly. Inset shows the ROC of C_γ edge weights threshold. **F)** Noise
589 (FP/TP ratio) as a function of TPR. **G)** The mean *iPLV* of TP or FP edges alone, and all edges.

590 **Fig 4**

591 *Hyperedge bundling outperformed raw edges.* **A)** The hypergraphs created with both clustering methods
592 were stable below CL of 0.4. **B)** The cumulative distribution function (cdf) of hyperedge size at different
593 levels of CL, computed with hyperedges pooled from 500 graphs with 100 iterations within each graph. For
594 both clustering methods **C)** and **D)**, increasingly strict hyperedge size threshold (θ_{HEsize} varying from 0 to 8)
595 caused separability and noise level (FP/TP) to decrease. **E,F)** The retained true positive raw edges also
596 decreased as hyperedge size threshold increased.
597

598 **Fig 5**

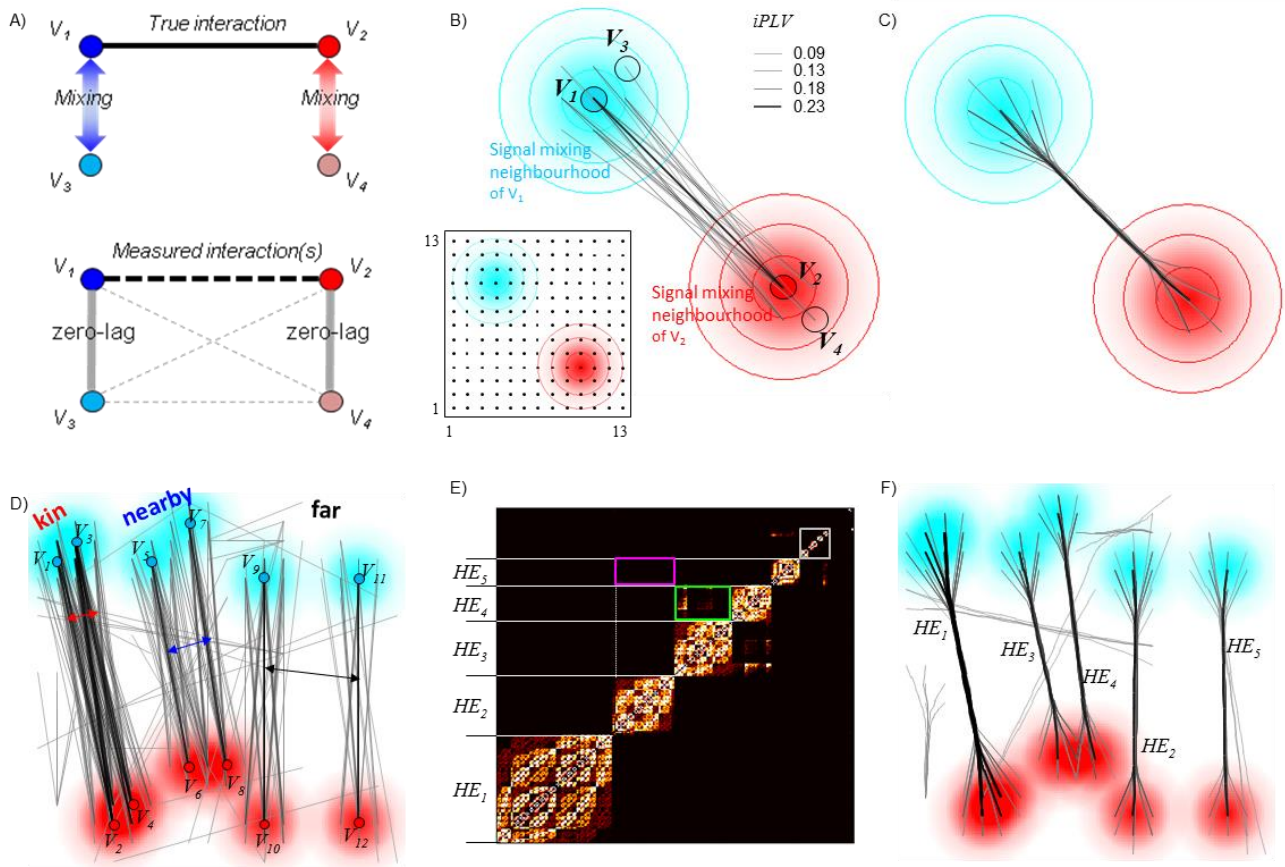
599 *Louvain clustering method yielded hypergraphs with lower noise but also lower separability than*
600 *UPGMA.* **A)** For CL values 0.15 – 0.45, Louvain hypergraphs had lower noise after singleton hyperedges were
601 deleted. **B)** True positive rate TPR was larger in Louvain hypergraphs for CL values 0.15 and 0.25 and larger
602 in UPGMA hypergraphs for CL values 0.35 and 0.45. **C)** Separability was higher for UPGMA method.

603 **Fig 6**

604 *Hypergraphs improve visualization of real and simulated data.* Visual crowding of numerous group-
605 level *iPLV* edges of 1:1 phase synchronization in **A)** alpha and **B)** gamma frequency band during VWM
606 retention (real MEG data), **C)** a simulated graph overlaid on a flattened 2D map of cortical regions. **D, E, F)**
607 Hypergraphs of **A,B,C)**. **D)** In alpha band, bundles of long-range hyperedges connect occipital and parietal
608 areas. Hyperedges were created with CL=0.15, $\theta_{HEsize}>6$. **E)** In gamma band, long-range hyperedges were
609 observed in the frontal and central regions. On these 2D map, different parcel colours indicate functional sub-
610 systems defined by (Yeo et al. 2011) and in hypergraphs, edge colours are obtained by mixing of the colours
611 of connected parcels. CN: cuneus; CS: central sulcus; iPGsup: supramarginal gyrus; mFG: middle frontal
612 gyrus; mOG: middle occipital gyrus; mOS: middle occipital sulcus and lunatus sulcus; laSp: posterior ramus;
613 prCG: precentral gyrus; pCIm: middle posterior cingulate; prCN: precuneus; sPG:superior parietal lobule; sOG:
614 superior occipital gyrus.
615
616
617
618
619

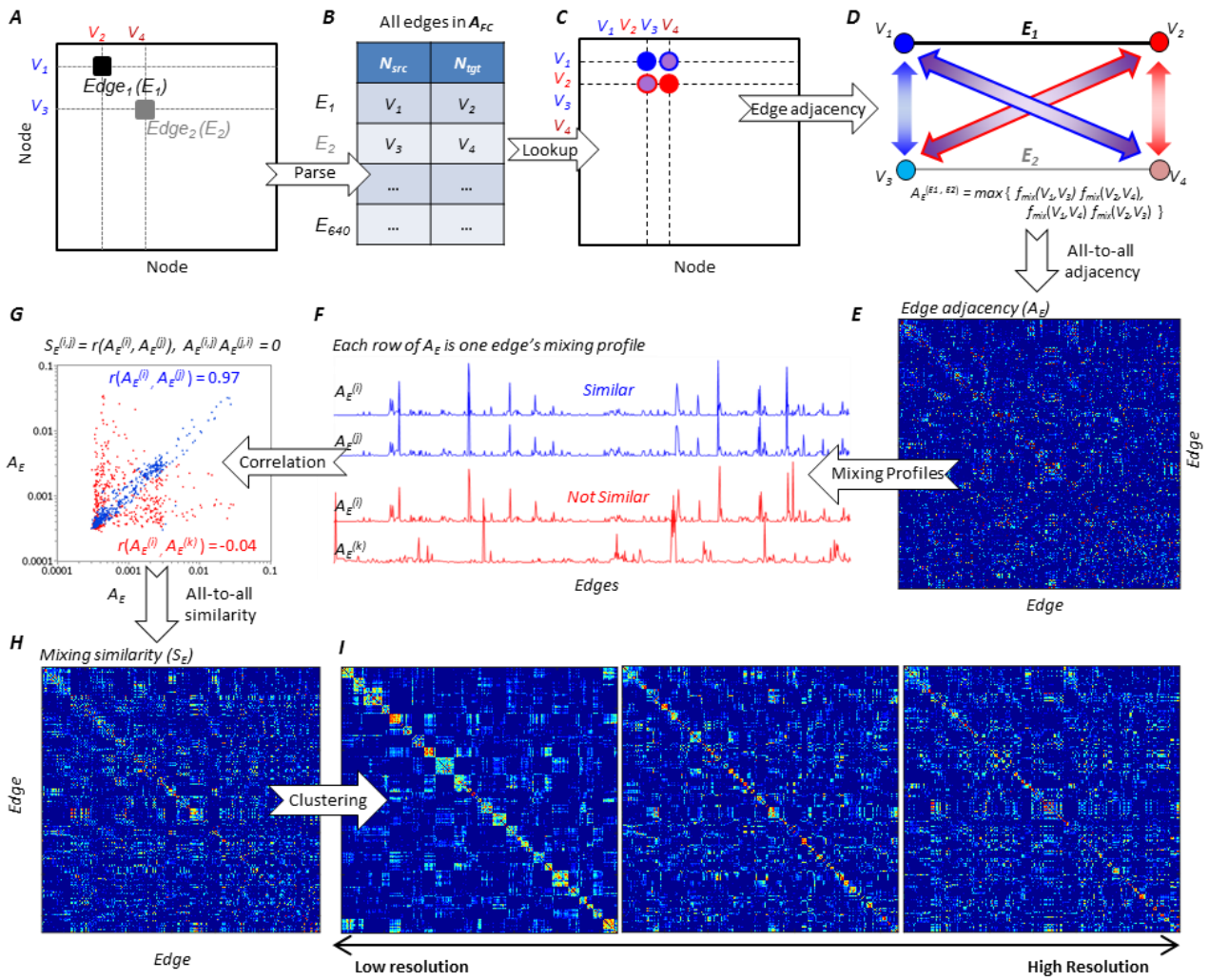
620 **8 Figures**

621 **Fig1**



622

623 Fig2

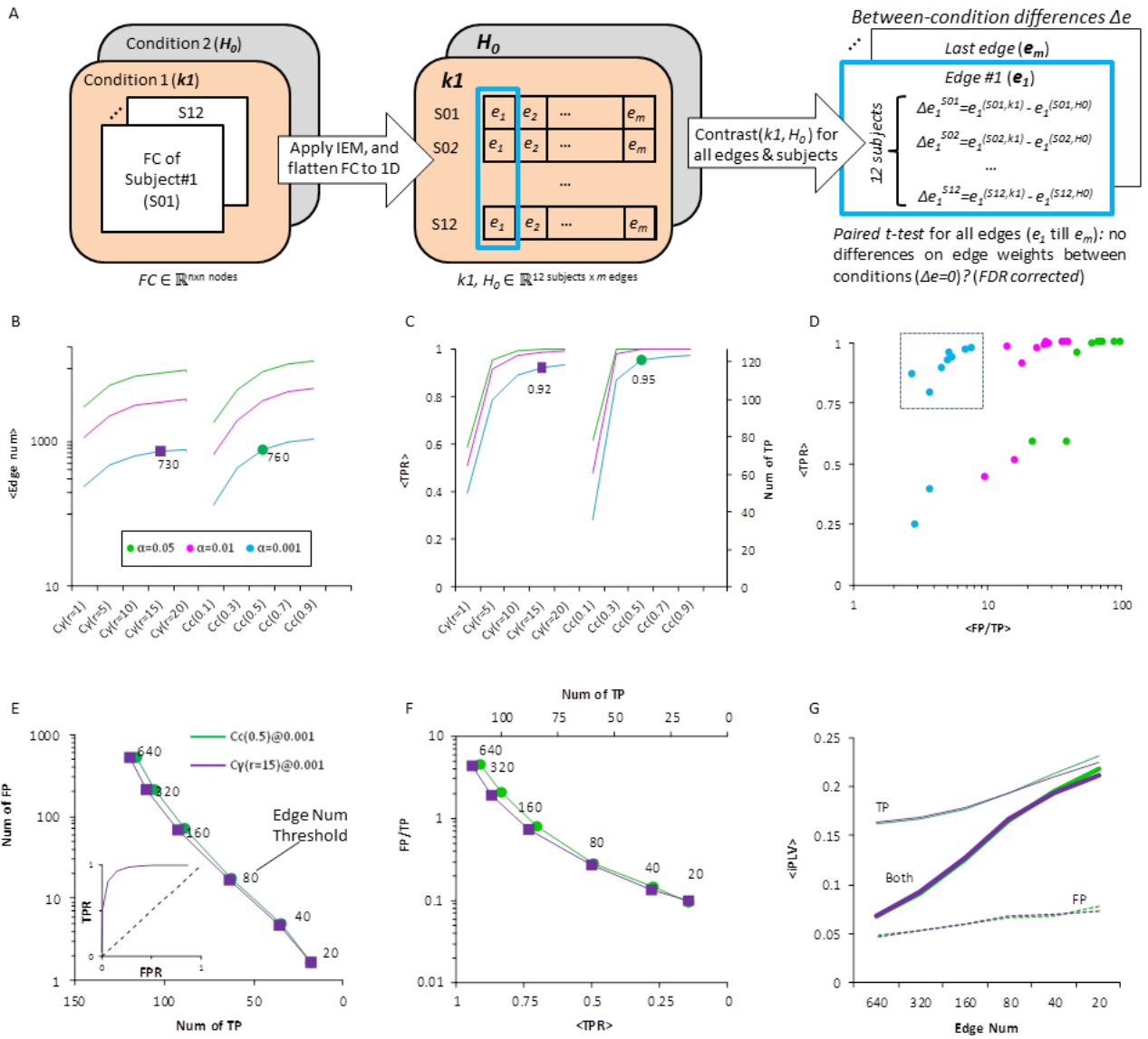


624

625

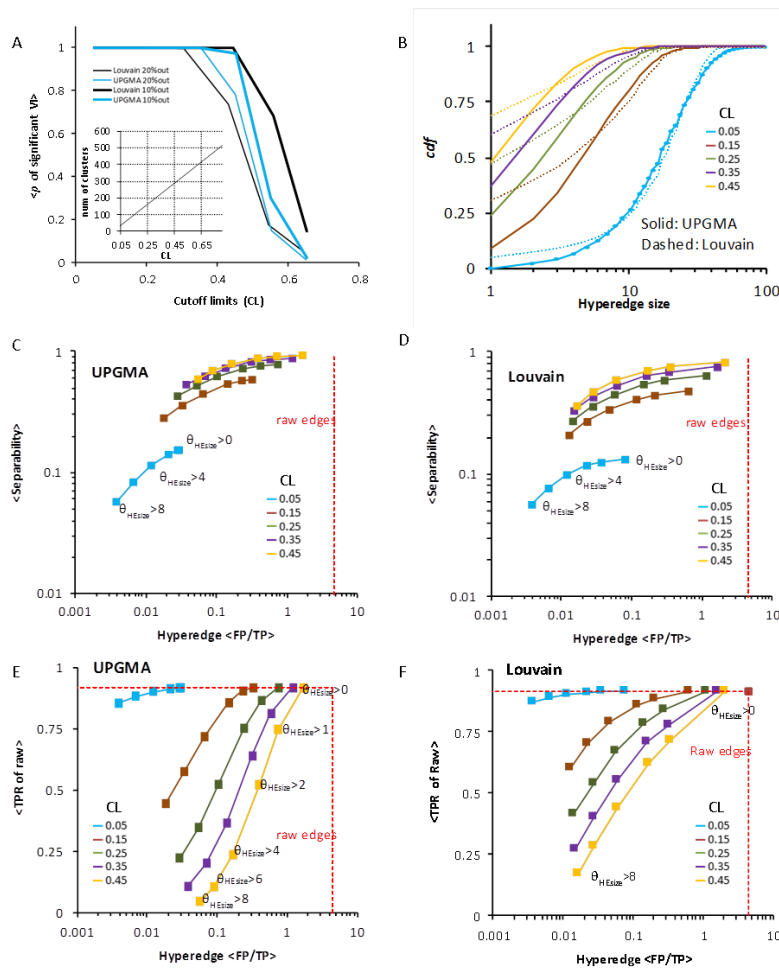
626

627 Fig3



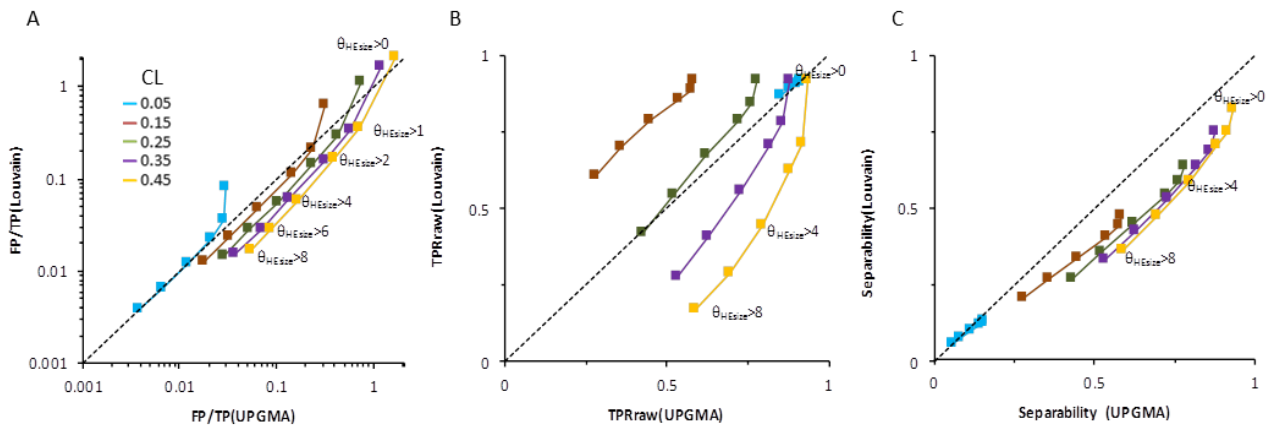
628

629 Fig4



630

631 Fig 5



632

633

References

- 634 Banerjee, O., El Ghaoui, L., d'Aspremont, A. (2008). Model selection through sparse maximum likelihood
635 estimation for multivariate gaussian or binary data. *J of Machine Learning Research*, 9, 485-516.
- 636 Bastos, A.M. and Schoffelen, J. (2016). A tutorial review of functional connectivity analysis methods and their
637 interpretational pitfalls. *Frontiers in Systems Neuroscience*, 9, 1662-5137.
- 638 Ben-Hur, A., Elisseeff, A., Guyon, I. (2002). A stability based method for discovering structure in clustered
639 data. *Pac Symp Biocomput.*, 6-17.
- 640 Blondel, V.D., Guillaume, J.L., Lambiotte, R., Lefebvre, E. (2008). Fast unfolding of communities in large
641 networks. *Journal of Statistical Mechanics: Theory and Experiment*, 2008, P10008.
- 642 Brookes, M.J., Woolrich, M.W., Barnes, G.R. (2012). Measuring functional connectivity in MEG: A
643 multivariate approach insensitive to linear source leakage. *NeuroImage*, 63, 910-920.
- 644 Brookes, M.J., Tewarie, P.K., Hunt, B.A.E., Robson, S.E., Gascoyne, L.E., Liddle, E.B., Liddle, P.F., Morris,
645 P.G. (2016). A multi-layer network approach to MEG connectivity analysis. *NeuroImage*, 132, 425-438.
- 646 Brookes, M.J., O'Neill, G.C., Hall, E.L., Woolrich, M.W., Baker, A., Palazzo Corner, S., Robson, S.E., Morris,
647 P.G., Barnes, G.R. (2014). Measuring temporal, spectral and spatial changes in electrophysiological brain
648 network connectivity. *NeuroImage*, 91, 282-299.
- 649 Bullmore, E. and Sporns, O. (2012). The economy of brain network organization. *Nature*
650 *Reviews.Neuroscience*, 13, 336-349.
- 651 Bullmore, E. and Sporns, O. (2009). Complex brain networks: Graph theoretical analysis of structural and
652 functional systems. *Nature Reviews.Neuroscience*, 10, 186-198.
- 653 Buzsaki, G., Anastassiou, C.A., Koch, C. (2012). The origin of extracellular fields and currents " EEG,
654 ECoG, LFP and spikes. *Nature Reviews Neuroscience*, 13, 407-420.
- 655 Colclough, G.L., Brookes, M.J., Smith, S.M., Woolrich, M.W. (2015). A symmetric multivariate leakage
656 correction for MEG connectomes. *NeuroImage*, 117, 439-448.
- 657 Colclough, G.L., Woolrich, M.W., Tewarie, P.K., Brookes, M.J., Quinn, A.J., Smith, S.M. (2016). How
658 reliable are MEG resting-state connectivity metrics? *NeuroImage*, 138, 284-293.

- 659 Drakesmith, M., El-Deredy, W., Welbourne, S. (2013). Reconstructing coherent networks from
660 electroencephalography and magnetoencephalography with reduced contamination from volume
661 conduction or magnetic field spread. *PLoS ONE*, 8, e81553.
- 662 Drakesmith, M., Caeyenberghs, K., Dutt, A., Lewis, G., David, A.S., Jones, D.K. (2015). Overcoming the
663 effects of false positives and threshold bias in graph theoretical analyses of neuroimaging data.
664 *NeuroImage*, 118, 313-333.
- 665 Everson, R. (1999). Orthogonal, but not orthonormal, procrustes problems. *Imperial College Technical Report*,
666 *TR99-6*.
- 667 Farahibozorg, S.R., Henson, R.N., Hauk, O. Adaptive cortical parcellations for source reconstructed
668 EEG/MEG connectomes. *BioRxiv Doi: 10.1101/123456*, .
- 669 Fornito, A., Zalesky, A., Breakspear, M. (2015). The connectomics of brain disorders. *Nature*
670 *Reviews.Neuroscience*, 16, 159-172.
- 671 Friedman, J., Hastie, T., Tibshirani, R. (2008). Sparse inverse covariance estimation with the graphical lasso.
672 *Biostatistics*, 9(3), 432-441.
- 673 Gross, J., Baillet, S., Barnes, G.R., Henson, R.N., Hillebrand, A., Jensen, O., Jerbi, K., Litvak, V., Maess, B.,
674 Oostenveld, R., Parkkonen, L., Taylor, J.R., van Wassenhove, V., Wibrals, M., Schoffelen, J.M. (2013).
675 Good practice for conducting and reporting MEG research. *NeuroImage*, 65, 349-363.
- 676 Hamalainen, M., Hari, R., Ilmoniemi, R.J., Knuutila, J., Lounasmaa, O.V. (1993).
677 Magnetoencephalography theory, instrumentation, and applications to noninvasive studies of the working
678 human brain. *Reviews of Modern Physics*, 65, 413-497.
- 679 Hamalainen, M.S. and Ilmoniemi, R.J. (1994). Interpreting magnetic fields of the brain: Minimum norm
680 estimates. *Medical & Biological Engineering & Computing*, 32, 35-42.
- 681 Hamalainen, M.S. and Sarvas, J. (1989). Realistic conductivity geometry model of the human head for
682 interpretation of neuromagnetic data. *IEEE Transactions on Bio-Medical Engineering*, 36, 165-171.
- 683 Hauk, O. and Stenroos, M. (2014). A framework for the design of flexible cross-talk functions for spatial
684 filtering of EEG/MEG data: DeFleCT. *Human Brain Mapping*, 35, 1642-1653.
- 685 Hauk, O., Wakeman, D.G., Henson, R. (2011). Comparison of noise-normalized minimum norm estimates for
686 MEG analysis using multiple resolution metrics. *NeuroImage*, 54, 1966-1974.

- 687 Haumann, N.T., Parkkonen, L., Kliuchko, M., Vuust, P., Brattico, E. (2016). Comparing the performance of
688 popular MEG/EEG artifact correction methods in an evoked-response study. *Computational Intelligence*
689 *and Neuroscience*, .
- 690 Hillebrand, A., Barnes, G.R., Bosboom, J.L., Berendse, H.W., Stam, C.J. (2012). Frequency-dependent
691 functional connectivity within resting-state networks: An atlas-based MEG beamformer solution.
692 *NeuroImage*, 59, 3909-3921.
- 693 Hincapié, A., Kujala, J., Mattout, J., Pascarella, A., Daligault, S., Delpuech, C., Mery, D., Cosmelli, D., Jerbi,
694 K. (2017). The impact of MEG source reconstruction method on source-space connectivity estimation: A
695 comparison between minimum-norm solution and beamforming. *NeuroImage*, 156, 29-42.
- 696 Hipp, J.F., Hawellek, D.J., Corbetta, M., Siegel, M., Engel, A.K. (2012). Large-scale cortical correlation
697 structure of spontaneous oscillatory activity. *Nature Neuroscience*, 15, 884-890.
- 698 Holten, D. and Wijk, J.J.V. (2009). Force-directed edge bundling for graph visualization. .
- 699 Jain, A.K., Murty, M.N., Flynn, P.J. (1999). Data clustering: A review. *ACM Comput.Surv.*, 31, 264-323.
- 700 Karl J., F. (2011). Functional and effective connectivity: A review. *Brain Connectivity*, 1 1, 13 -36.
- 701 Kreuz, T. (2011). Measures of neuronal signal synchrony. *Scholarpedia*, 6, 11922.
- 702 Kujala, J., Gross, J., Salmelin, R. (2008). Localization of correlated network activity at the cortical level with
703 MEG. *NeuroImage*, 39, 1706-1720.
- 704 Lin, F.H., Witzel, T., Ahlfors, S.P., Stufflebeam, S.M., Belliveau, J.W., Hamalainen, M.S. (2006). Assessing
705 and improving the spatial accuracy in MEG source localization by depth-weighted minimum-norm
706 estimates. *NeuroImage*, 31, 160-171.
- 707 Liu, A.K., Dale, A.M., Belliveau, J.W. (2002). Monte carlo simulation studies of EEG and MEG localization
708 accuracy. *Human Brain Mapping*, 16, 47-62.
- 709 Lobier, M., Palva, J.M., Palva, S. (2017). High-alpha band synchronization across frontal, parietal and visual
710 cortex mediates behavioral and neuronal effects of visuospatial attention. *NeuroImage*, 165, 222-237.
- 711 Löwdin, P.O. (1950). On the nonorthogonality problem connected with the use of atomic
712 wave functions in the theory of molecules and crystals. *J. Chem. Phys.*, 18, 365–375.

- 713 Mannino, M. and Bressler, S.L. (2015). Foundational perspectives on causality in large-scale brain networks.
714 *Physics of Life Reviews*, 15, 107-123.
- 715 Marrelec, G., Krainik, A., Duffau, H., Pélégrini-Issac, M., Lehericy, S., Doyon, J., Benali, H. (2006). Partial
716 correlation for functional brain interactivity investigation in functional MRI. *NeuroImage*, 32, 228-237.
- 717 Meilă, M. (2007). Comparing clusterings—an information based distance. *Journal of Multivariate Analysis*,
718 98, 873-895.
- 719 Nolte, G., Bai, O., Wheaton, L., Mari, Z., Vorbach, S., Hallett, M. (2004). Identifying true brain interaction
720 from EEG data using the imaginary part of coherency. *Clinical Neurophysiology : Official Journal of the*
721 *International Federation of Clinical Neurophysiology*, 115, 2292-2307.
- 722 O'Neill, G.C., Barratt, E.L., Hunt, B.A., Tewarie, P.K., Brookes, M.J. (2015). Measuring electrophysiological
723 connectivity by power envelope correlation: A technical review on MEG methods. *Phys Med Biol.*,
724 60(21), 271-95.
- 725 Palva, S. and Palva, J.M. (2012). Discovering oscillatory interaction networks with M/EEG: Challenges and
726 breakthroughs. *Trends in Cognitive Sciences*, 16, 219-230.
- 727 Papo, D., Buld\u00f3 Javier M., Boccaletti, S., Bullmore, E.T. (2014). Complex network theory and the brain.
728 *Philosophical Transactions of the Royal Society of London B: Biological Sciences*, 369.
- 729 Petersen, S. . and Sporns, O. (2015). Brain networks and cognitive architectures. *Neuron*, 88, 207-219.
- 730 Preti, M.G., Bolton, T.A., Van De Ville, D. (2016). The dynamic functional connectome: State-of-the-art and
731 perspectives. *NeuroImage*, .
- 732 Rubinov, M. and Sporns, O. (2010). Complex network measures of brain connectivity: Uses and
733 interpretations. *NeuroImage*, 52, 1059-1069.
- 734 Rubinov, M. (2015). Neural networks in the future of neuroscience research. *Nature Reviews. Neuroscience*,
735 *advance online publication*, 1471-0048.
- 736 S. Baillet, J. C. Mosher, R. M. Leahy. (2001). Electromagnetic brain mapping. *IEEE Signal Processing*
737 *Magazine*, 18, 14-30.
- 738 Salmelin, R. and Baillet, S. (2009). Electromagnetic brain imaging. *Human Brain Mapping*, 30, 1753-1757.

- 739 Santarnecchi, E., Galli, G., Polizzotto, N.R., Rossi, A., Rossi, S. (2014). Efficiency of weak brain connections
740 support general cognitive functioning. *Human Brain Mapping*, 35, 4566–4582.
- 741 Schoffelen, J.M. and Gross, J. (2009). Source connectivity analysis with MEG and EEG. *Human Brain*
742 *Mapping*, 30, 1857-1865.
- 743 Siebenhühner, F., Wang, S.H., Palva, J.M., Palva, S. (2016). Cross-frequency synchronization connects
744 networks of fast and slow oscillations during visual working memory maintenance. *ELife*, 5,
745 10.7554/eLife.13451.
- 746 Sporns, O., Tononi, G., Kotter, R. (2005). The human connectome: A structural description of the human brain.
747 *PLoS Computational Biology*, 1, e42.
- 748 Sporns, O. (2014). Contributions and challenges for network models in cognitive neuroscience. *Nature*
749 *Neuroscience*, 17, 652-660.
- 750 Uhlhaas, P.J. and Singer, W. (2010). Abnormal neural oscillations and synchrony in schizophrenia. *Nat Rev*
751 *Neurosci*, 11, 100-113.
- 752 Uhlhaas, P.J. and Singer, W. (2006). Neural synchrony in brain disorders: Relevance for cognitive
753 dysfunctions and pathophysiology. *Neuron*, 52, 155-168.
- 754 van Wijk, Bernadette C. M., Stam, C.J., Daffertshofer, A. (2010). Comparing brain networks of different size
755 and connectivity density using graph theory. *PLoS ONE*, 5, e13701.
- 756 Wens, V. (2015). Investigating complex networks with inverse models: Analytical aspects of spatial leakage
757 and connectivity estimation. *91*, 17.
- 758 Williams, N.J., Nasuto, S.J., Saddy, J.D. (2015). Method for exploratory cluster analysis and visualisation of
759 single-trial ERP ensembles. *Journal of Neuroscience Methods*, 250, 22-33.
- 760 Wollstadt, P., Meyer, U., Wibral, M. (2015). **A graph algorithmic approach to separate direct from**
761 **indirect neural interactions.** *PLOS One*, *arXiv:1504.00156*.
- 762 Zalesky, A., Fornito, A., Cocchi, L., Gollo, L.L., Breakspear, M. (2014). Time-resolved resting-state brain
763 networks. *Proceedings of the National Academy of Sciences of the United States of America*, 111, 10341-
764 10346.
- 765 Zhigalov, A., Arnulfo, G., Nobili, L., Palva, S., Palva, J.M. (2017). Modular co-organization of functional
766 connectivity and scale-free dynamics in the human brain. *Network Neuroscience*, 1.

